

# Support Vector Machine for Multifrequency SAR Polarimetric Data Classification

Cédric Lardeux, Pierre-Louis Frison, Céline Tison, Jean-Claude Souyris,  
Benoît Stoll, Bénédicte Fruneau, and Jean-Paul Rudant

**Abstract**—The objective of this paper is twofold: first, to assess the potential of radar data for tropical vegetation cartography and, second, to evaluate the contribution of different polarimetric indicators that can be derived from a fully polarimetric data set. Because of its ability to take numerous and heterogeneous parameters into account, such as the various polarimetric indicators under consideration, a support vector machine (SVM) algorithm is used in the classification step. The contribution of the different polarimetric indicators is estimated through a greedy forward and backward method. Results have been assessed with AIRSAR polarimetric data polarimetric data acquired over a dense tropical environment. The results are compared to those obtained with the standard Wishart approach, for single frequency and multifrequency bands. It is shown that, when radar data do not satisfy the Wishart distribution, the SVM algorithm performs much better than the Wishart approach, when applied to an optimized set of polarimetric indicators.

**Index Terms**—Polarimetry, supervised classification, support vector machine (SVM), synthetic aperture radar (SAR), tropical vegetation.

## I. INTRODUCTION

**P**OLARIZATION diversity has been uncommon in spaceborne synthetic aperture radar (SAR) of the last century. Most civilian systems were designed to transmit a single waveform in terms of polarization, such as the ERS-1 and -2 satellites (vertical linear polarization) or RADARSAT-1 and JERS (horizontal linear polarization). New space missions, however, all include operational or experimental polarimetric modes to various extents. For the first time, ASAR/ENVISAT (launched in March 2002) was given a limited polarization diversity. The current situation has changed rapidly with the launch of full or partial polarimetry payloads [RADARSAT-2,

TERRASAR-X, and ALOS], using C-, X-, and L-bands, respectively, for resolutions ranging from 3 to 10 m.

Polarimetric information is of prime interest for classification purposes. When full polarimetry is available, basically two families of algorithms can be used: on one hand, those that decompose a backscatter wave into standard backscattering mechanisms (simple, double, helix, volume scattering, ...), e.g., Pauli decomposition and Freeman and Durden [1] or Krogager decomposition [2], and, on the other hand, algebraic approaches, based on the eigenvalue and eigenvectors analysis of the coherency matrix [3], from which parameters such as entropy  $H$ , the main average scattering mechanism  $\alpha$ , and anisotropy are inferred. In addition to these familiar polarimetric tools, other analysis tools allow one to calculate the transmission and reception polarizations that maximize polarimetric contrast [4]. Classification can also be achieved using the Bayes theory and the complex Wishart distribution of the covariance matrix elements [5]. More recently, the merging of decomposition techniques with a Wishart classifier was proposed to conduct unsupervised classification [6].

Finally, various polarimetric indicators were used in other classification schemes, such as neural networks [7], hierarchical classifiers [8], or classifiers based on wavelet transform [9]. The magnitudes of the linearly polarized radar responses ( $|hh|$ ,  $|hv|$ , and  $|\nu\nu|$ ) acquired at one or several frequencies are generally used in conjunction with other indicators, such as their ratio, the degree of coherence  $\rho$  between  $hh$  and  $\nu\nu$  complex responses, or a variation coefficient characterizing the local texture in each polarization channel [10]. Other references use circular or linear radar response ratios for surface/volume scattering discrimination when a subsurface is prospected [11]. Mattia *et al.* [12] have shown the added value of the degree of coherence expressed in a basis of circular polarizations for surface roughness characterization. Finally, other polarimetric indicators based on the extremes of the degree of polarization or the intensity of free-space backscattered power have also been pointed out [13].

The aim of this paper is twofold: First, it is to assess the potential of radar polarimetric data for land use classification over a tropical environment. Second, it is to evaluate the contribution of different polarimetric indicators for such application. To this end, a support vector machine (SVM) classification method is used since it is well suited to handle linearly nonseparable cases by using the Kernel theory [14]. Among other advantages, this method allows defining feature vectors with numerous and heterogeneous components. It has been mostly applied to hyperspectral remotely sensed data, and a few studies have also been carried out on SAR data [15], [16]. The various polarimetric

Manuscript received December 10, 2007; revised June 18, 2008, November 17, 2008, and March 18, 2009. First published September 22, 2009; current version published November 25, 2009.

C. Lardeux is with the Laboratoire Géomatériaux et Géologie de l'Ingénieur, Institut Francilien des Sciences Appliquées, Université Paris-Est, 77 454 Marne-la-Vallée, France, and also with the SAPHIR Team, Université de Rennes, 35042 Rennes cedex, France.

P.-L. Frison, B. Fruneau, and J.-P. Rudant are with the Laboratoire Géomatériaux et Géologie de l'Ingénieur, Institut Francilien des Sciences Appliquées, Université Paris-Est, 77 454 Marne-la-Vallée, France (e-mail: frison@univ-mlv.fr).

C. Tison and J.-C. Souyris are with the Altimetry and Radar Department, Centre National d'Etudes Spatiales, 31401 Toulouse, France (e-mail: celine.tison@cnes.fr; jean-claude.souyris@cnes.fr).

B. Stoll is with Laboratoire des Géosciences du Pacifique Sud, Université de Polynésie Française, 98702 Tahiti, Polynésie Française (e-mail: benoit.stoll@upf.pf).

Color versions of one or more of the figures in this paper are available online at <http://ieeexplore.ieee.org>.

Digital Object Identifier 10.1109/TGRS.2009.2023908

indicators are selected through a stepwise process. Unlike algorithms such as principal component analysis that is already investigated for polarimetric SAR data [17], this method keeps the feature vector unchanged, allowing for an easier physical interpretation of results.

The method is applied to fully polarimetric L- and P-band data and  $\nu\nu$  polarized C-band data, which have been collected in August 2000 by the Jet Propulsion Laboratory (JPL)–AIRSAR sensor over the Tubuai Island, French Polynesia.

First, the SVM algorithm is assessed with a feature vector composed of the nine real elements of the coherency matrix. The results are compared to those obtained with a standard classification based on the complex Wishart distribution [5]. Subsequently, the contribution of different polarimetric indicators is investigated in single frequency cases and when P-, L-, and C-band data are merged together.

The developed methodology, i.e., the different polarimetric indicators investigated, the SVM algorithm, and greedy methods used to assess the polarimetric indicator contribution are introduced in the second section. Section III is dedicated to the experimental results: First, the data used and study site are presented. Then, the results involving single or multiple frequency bands are discussed in the light of their comparison to Wishart classification. Section IV summarizes our conclusions and draws perspectives.

## II. METHODOLOGY

### A. Polarimetric Indicators

The coherency matrix  $T$  is defined from a scattering target vector  $k_p$  expressed in the Pauli basis as follows [18]:

$$k_p = \frac{1}{\sqrt{2}} \begin{pmatrix} S_{hh} + S_{\nu\nu} \\ S_{hh} - S_{\nu\nu} \\ 2S_{h\nu} \end{pmatrix} \quad T = \langle k_p k_p^{*T} \rangle \quad (1)$$

where  $S_{pq}$  denotes the scattering matrix element corresponding to the  $p-q$  polarization of a receiving–transmitting wave ( $p$  and  $q$  referring to horizontal  $h$  or vertical  $\nu$  linear polarization), and  $\langle \rangle$  stands for the spatial averaging during the multilook processing. In addition to the coherency matrix terms  $T_{ij}$ , various polarimetric indicators can be derived from a polarimetric measurement. They are detailed as follows and summarized in Table I.

- 1) The intensities of the copolarized channel in linear and circular polarizations:  $I_{pp} = |S_{pp}|^2$ , where  $p$  refers to  $h$ ,  $\nu$ ,  $l$ , or  $r$  (for linear horizontal, vertical, circular left, or right polarization respectively). It can be noted that the cross-polarized channels  $I_{h\nu}$  and  $I_{lr}$  correspond to the coherency matrix elements  $T_{33}$  and  $T_{11}$ , respectively, and are not retained to avoid redundancy.
- 2) The Span:  $S = I_{hh} + 2I_{h\nu} + I_{\nu\nu}$ .
- 3) The local heterogeneity is taken into account through the coefficient of variation  $c_\nu = (\sigma/\mu)$ , where  $\sigma$  and  $\mu$  represent the standard deviation and mean estimated over a  $5 \times 5$  neighborhood for a given radiometric channel, respectively.  $c_{\nu-pq}$  represents the coefficient of variation associated to a transmission in  $q$  polarization and a re-

TABLE I  
POLARIMETRIC INDICATORS ASSESSED FOR CLASSIFICATION

Description	Designation
Elements of the coherency matrix (modulus and arguments)	$T_{ij}$ ( $i, j = 1, 2, 3$ )
Linear and circular intensities	$I_{hh}, I_{\nu\nu}, I_{ll}, I_{rr}$
Span	$S = I_{hh}^2 + 2 I_{h\nu}^2 + I_{\nu\nu}^2$
Linear and circular intensities ratio	$I_{h\nu}/I_{\nu\nu}, I_{h\nu}/I_{hh}, I_{hh}/I_{\nu\nu}, I_{rr}/I_{ll}, I_{ll}/I_{lr}, I_{ll}/I_{rr}$
Degree of coherence between linear polarizations (Modulus and Argument)	$\rho_{hh-\nu\nu}, \rho_{hh-h\nu}, \rho_{\nu\nu-h\nu}$
Degree of coherence between circular polarizations (Modulus and Argument)	$\rho_{ll-rr}, \rho_{ll-lr}, \rho_{rr-lr}$
Extremes of the backscattered intensity	$I_{\min}, I_{\max} / I_{\min}$
Extremes of the degree of polarization	$d_{-P_{\min}}, d_{-P_{\max}}, \Delta(d_{-P})$
Linear and circular coefficient of variation	$c_{\nu-\nu\nu}, c_{\nu-h\nu}, c_{\nu-hh}, c_{\nu-ll}, c_{\nu-lr}, c_{\nu-rr}$
Euler parameters	$m, \gamma, \psi, \nu, \tau$
Entropy, anisotropy, $\alpha$ parameter	$H/a/\alpha$
Freeman decomposition parameters	$P_s, P_d, P_v$

ception in  $p$  polarization (linear and circular polarizations will be considered).

- 4) The ratio between different intensity channels in linear and circular polarization bases

$$\frac{I_{h\nu}}{I_{hh}}, \quad \frac{I_{h\nu}}{I_{\nu\nu}}, \quad \frac{I_{hh}}{I_{\nu\nu}}, \quad \frac{I_{ll}}{I_{lr}}, \quad \frac{I_{rr}}{I_{lr}}, \quad \frac{I_{ll}}{I_{rr}}.$$

In particular, the indicators  $I_{h\nu}/I_{hh}$  and  $I_{lr}/I_{ll}$  are used in planetology to discriminate between surface and volume scattering mechanisms [19].

- 5) The modulus and phase of the polarimetric degree of coherence  $\rho_{hh-\nu\nu}, \rho_{h\nu-\nu\nu}, \rho_{h\nu-hh}, \rho_{ll-lr}, \rho_{rr-lr}$ , and  $\rho_{ll-rr}$ , computed over a  $5 \times 5$  neighborhood as follows:

$$\rho_{pq-p'q'} = \frac{\langle S_{pq} S_{p'q'}^* \rangle}{\sqrt{\langle |S_{pq}|^2 \rangle \cdot \langle |S_{p'q'}|^2 \rangle}} = |\rho_{pq-p'q'}| e^{j\varphi_{pq-p'q'}}$$

where  $p, q, p'$ , or  $q'$  stands for  $h, \nu, l$ , or  $r$  polarization.

- 6) Accounting for the different approaches that allow for the optimization of the free-space backscattered power contrast [13], its minimum  $I_{\min}$  and maximum  $I_{\max}$  are calculated when the transmitted polarization takes any value on the Poincaré sphere.  $I_{\min}$  and the ratio  $I_{\min}/I_{\max}$  are retained. Due to the high correlation observed between the Span and  $I_{\max}$  over the whole scene ( $r^2 = 0.99$  for 1 786 701 points), the latter is not selected.
- 7) The minimum  $d_{-P_{\min}}$  and the maximum  $d_{-P_{\max}}$  of the degree of polarization of the free-space backscattered wave are also calculated when the transmitted polarization takes any value on the Poincaré sphere. The degree of polarization is defined as  $d_{-P} = (\sqrt{S_2^2 + S_3^2 + S_4^2}/S_1)$ , where  $S_i$  denotes the components of 4-D Stokes vector [20].  $d_{-P_{\min}}$  and  $d_{-P_{\max}}$  are retained, as well as their difference  $\Delta(d_{-P})$ .

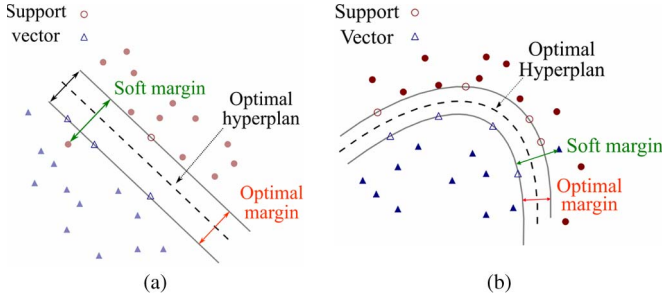


Fig. 1. SVM classifier scheme. (a) Linear and (b) nonlinear cases.

- 8) The three parameters  $H/A/\alpha$  representing the entropy (an indication of the respective weights of the polarized and unpolarized components in the makeup of the backscattered wave), the scattering mechanism, and the anisotropy inferred from the coherency matrix [3].
- 9) The three intensity parameters of the Freeman decomposition  $P_s$ ,  $P_d$ , and  $P_v$ , corresponding to the weight of single, double, and volume in the backscattered response [1].
- 10) The five Euler parameters  $\gamma$ ,  $\nu$ ,  $\tau$ ,  $\psi$ , and  $m$  associated to the characteristic polarizations of the polarimetric signatures [21]. These parameters are here derived from the matrix of coherence  $T$ , according to the method described by Laurent *et al.* [22]. It assumes the following coherency matrix decomposition:  $T = T^{\text{pol}} + T^{\text{unpol}}$ , where  $T^{\text{pol}}$  and  $T^{\text{unpol}}$  represent the polarized and unpolarized parts of the backscattered response, respectively. The Euler parameters are estimated from  $T^{\text{pol}}$ .

Details about the distributions observed by these different polarimetric indicators over natural surfaces can be found in [23]–[25].

### B. SVM Method

A brief description of the SVM is given hereinafter, and more details can be found in [14]. The first part presents the method in a linear case, followed by the extension to nonlinear case. Fig. 1 shows an illustration of the description made hereinafter.

1) *Linear Case*: Let us consider a two-class classification problem with  $P$  training samples. Each sample is described by an  $N$  dimension vector  $V_j^{(N)} = V_j$  ( $j \leq P$ ), belonging to an input space  $E$  (with the same dimension  $N$ ). The  $N$  vector components are also called primitives or, in the present case, polarimetric indicators. The label of the  $j$ th sample  $V_j$  is  $Y_j$ . For a two-class problem, the class labels are  $-1$  or  $+1$  (i.e.,  $Y_j \in \{-1; +1\}$ ).

The classification problem consists in finding an optimal hyperplane (i.e., a subspace of dimension  $N - 1$ ), for separating the two classes. Such a hyperplane is defined by its normal vector  $\omega$  and an offset  $b$ . A classification function  $f$  defining the label  $Y_j$  of the sample  $V_j$  is defined by

$$f(V_j) = \text{Sign}((\omega \cdot V_j) + b) = Y_j \quad (2)$$

where  $\text{Sign}$  is the sign function, and  $(\omega \cdot V_j)$  represents the scalar product between  $\omega$  and  $V_j$ . A vector subset corresponding to the training samples which are closest to the considered hyperplane

is called the support vector [Fig. 1(a)]. The distance between the support vector and the considered hyperplane is called the margin and is equal to  $1/\|\omega\|$ , where  $\|\omega\|$  refers to the norm of  $\omega$  vector. The goal of the SVM is to compute the optimal hyperplane separating the two classes or, equivalently, to maximize the margin by finding the  $\min(\|\omega\|)$ . This optimization is performed through the Lagrangian formalism

$$f(V_j) = \text{Sign} \left( \sum_{i=1}^P Y_i \cdot \alpha_i \cdot (\omega \cdot V_j) + b \right) \quad (3)$$

where  $\alpha_i$  denotes the Lagrange multipliers.

The presence of noise in the data can be accounted for by defining a distance tolerating the data scattering, thus relaxing the decision constraint. The considered distance is named the cost parameter  $C$ , and the optimal margin is, in this case, rather called the soft margin.

2) *Nonlinear Case*: When no hyperplane can be found in the input space  $E$  between the two classes [Fig. 1(b)], training vectors are projected into a space  $H$  of dimension  $M$  ( $M > N$ ), named the feature space to go back to a linear problem. The projection is realized through a projection function  $\Phi(\Phi: \mathbb{R}^N \mapsto H)$ . In this case, the classification function (3) becomes

$$f(V_j) = \text{Sign} \left( \sum_{i=1}^P Y_i \cdot \alpha_i \cdot (\Phi(V_j) \cdot \Phi(V_i)) + b \right). \quad (4)$$

The analytical form of  $\Phi$  is not required, as only its scalar product  $(\Phi(V_j) \cdot \Phi(V_i))$  appears in (4).  $(\Phi(V_j) \cdot \Phi(V_i))$  is called the Kernel function  $K$

$$K(V_j, V_i) = (\Phi(V_j) \cdot \Phi(V_i)). \quad (5)$$

From (4) and (5), we have  $f(V_j) = \text{Sign}(\sum_{i=1}^P Y_i \cdot \alpha_i \cdot K(V_j, V_i) + b)$ .

This formalism enables an easy change of computation space (the features are not really projected to get the hyperplane).

The following three types of kernels are commonly used:

- 1) a polynomial kernel  $K(V, V_i) = ((V \cdot V_i) + 1)^p$ ;
- 2) a sigmoid kernel  $K(V, V_i) = \tanh((V \cdot V_i) + 1)$ ;
- 3) a radial basis function (RBF) kernel

$$K(V, V_i) = \exp - \frac{|V - V_i|^2}{2\sigma^2}.$$

The principle of SVM has been developed for a two-class problem but can be easily extended to a multiclass problem by considering, for example, “One Against All” (OAA) or “One Against One” (OAO) algorithms [26]. If  $Q$  classes are to be considered, the OAA algorithm consists in the construction of  $Q$  hyperplanes that separate respectively one class and the  $Q - 1$  other classes. The OAO algorithm consists in the construction of  $Q(Q - 1)/2$  hyperplanes which separate each pair of classes. In this case, the final label is the one which has been chosen the most often, while for the OAA algorithm, the final label is corresponding to the largest margin. After several tests, the OAO algorithm has been retained.

### C. Greedy Analysis

This section develops the method used to assess the contribution of the different polarimetric indicators mentioned in Section II-A for classification. Ideally, the best combination defined by  $p$  chosen among  $N$  polarimetric indicators would be derived by testing all  $C_N^p$  possible combinations. However, this is unrealistic due to the time needed for computation. Consequently, an iterative algorithm based on the so-called greedy methods [27] is developed. In the following,  $E$  is the set of all the indicators which have been defined previously and  $V_{ref}^{(N_F)}$  a reference vector, which is defined with indicators that constitute a subset  $F \subseteq E$ .  $N_F$  and  $N_E$  are the cardinals of  $F$  and  $E$ .

Two goals have to be fulfilled. First, the contribution of the indicators belonging to  $V_{ref}^{(N_F)}$  should be assessed. This is done through a greedy backward method, which removes step by step the less efficient components in  $V_{ref}^{(N_F)}$ . Second, the additional indicators (those which belong to  $E - F$  set) should be added to  $V_{ref}^{(N_F)}$  in order to check whether they improve the classification or not. This is performed with a greedy forward analysis that selects step by step the most discriminating indicators belonging to the subset  $E - F$ .

The greedy backward analysis is implemented as follows: The SVM algorithm is applied to the  $N_F$  vectors of dimension  $N_F - 1$ ,  $V_{ref}^{(N_F-1)}$ , derived from  $V_{ref}^{(N_F)}$  once one primitive among the  $N_F$  has been removed. The resulting largest classification performance leads to the optimized vector of dimension  $N_F - 1$ , this latter being substituted to  $V_{ref}^{(N_F)}$  to initiate the second iteration. At step  $k$ , a vector  $V_{ref}^{(N_F-k)}$  is determined from  $V_{ref}^{(N_F-k+1)}$ , where  $V_{ref}^{(N_F-k)}$  gathers the  $N_F - k$  most efficient polarimetric indicators. It can be noted that the recursive feature extraction algorithm [27] was not assessed here as it is mostly useful for linear SVM situations, whereas the RBF kernel has been selected here.

The greedy forward analysis is performed as follows: The SVM algorithm is applied to the  $N_E - N_F$  vectors of dimension  $N_F + 1$ , derived from  $V_{ref}^{(N_F)}$  by the addition of one primitive belonging to the  $E - F$  subset to the  $N_F$  components of  $V_{ref}^{(N_F)}$ . The resulting highest classification accuracy leads to the optimized vector of dimension  $N_F + 1$ ,  $V_{ref}^{(N_F+1)}$ , which is used to initiate the second iteration. At step  $k$ , a vector  $V_{ref}^{(N_F+k)}$ , derived from  $V_{ref}^{(N_F+k-1)}$ , gathers the  $N_F + k$  most efficient polarimetric indicators given the initial configuration  $V_{ref}^{(N_F)}$ .

## III. APPLICATION

The proposed method is applied to AIRSAR polarimetric data acquired over the French Polynesian Tubuai Island, in order to assess the potential of radar polarimetric data for natural vegetation cartography. This section presents the study area and data used. Then, the results are analyzed.

### A. Study Area

Tubuai Island presents a large diversity of land use classes and vegetation types and is widely documented through regular

TABLE II  
LAND USE OF THE TUBUAI ISLAND

Class type	Class number - name	Percent t cover	# training samples	# control samples
Forest	1 - Pinus	13 %	3 000	5 000
	2 - Falcata	7 %	2 000	2 000
	3 - Purau	26 %	3 000	5 000
	4 - Guava	< 1 %	500	500
Low vegetation	5 - Fern lands	42%	2 000	2 500
	6 - Swampy vegetation	5%	2 000	5 000
Bare soils, roads	7 - Bare soils	5 %	2 000	5 000

*in situ* surveys. Tubuai is part of the *Australe* islands and is located at 23.38° S and 149.45° W, in the south of French Polynesia. It sustains a population of 6000 people with an area of 45 km<sup>2</sup>, presenting two little mountain chains whose highest point is 422 m high. Land use classes are listed in Table II. The habitat area, scattered over the island shore, does not appear because it is too small (< 1% of the island area), heterogeneous, and out of the scope of the study. Vegetation occupies 94% of the island with forest and low vegetation that are equally shared out. The forests spread over three main species: "Purau," "Pinus," and "Falcata," with some few "Strawberry Guava" specie patches (< 1%). The latter is particularly watched as it is an invasive species, coming from South America in 1840 and which was inventoried for the first time in 1979 in the Tubuai island (G. Paulay, personal communication). Low vegetation mainly consists in fern lands and swampy vegetation. Several ground surveys have been carried out, and their combination with a Quickbird image (cf. Section III-B2) allows the constitution of a valuable validation data set.

### B. Remotely Sensed Data

1) *AIRSAR Data*: For management purposes and the monitoring of different invasive vegetation species, the local administration authorities ordered an AIRSAR campaign in order to set up the cartography and the inventory of Polynesian landscape. The JPL-AIRSAR data were acquired in August 2000 at P-, L-, and C-band frequencies (430 MHz, 1.24 GHz, and 5.29 GHz, respectively). Fully polarimetric data are available at P- and L-band frequencies, while C-band data were only acquired in  $\nu\nu$  polarization. Fully polarimetric calibrated products are delivered as multilook complex format consisting in compressed Stokes matrix [28]. This calibration procedure concerns the correction of relative amplitudes and phases, as well as system cross talk [29]. The slant range resolution is 5.5 m for the three bands, and the azimuth resolution is 10.8, 13.5, and 31.5 m, respectively, for C-, L-, and P-bands. For the three bands, delivered data correspond to  $9 \times 1$  look in the azimuth and range directions, respectively, with a pixel size of  $5 \times 5$  m<sup>2</sup>. The incidence angle ranges between 26° and 62°.

Slight additional adjustments were performed on the polarimetric differential phases following Zebker *et al.* [30], in order to come up with centered normal histogram over the sea for  $\varphi_{hh} - \varphi_{\nu\nu}$ . In addition to that, a calibration coefficient has been applied to each of the linearly polarized intensity channels,



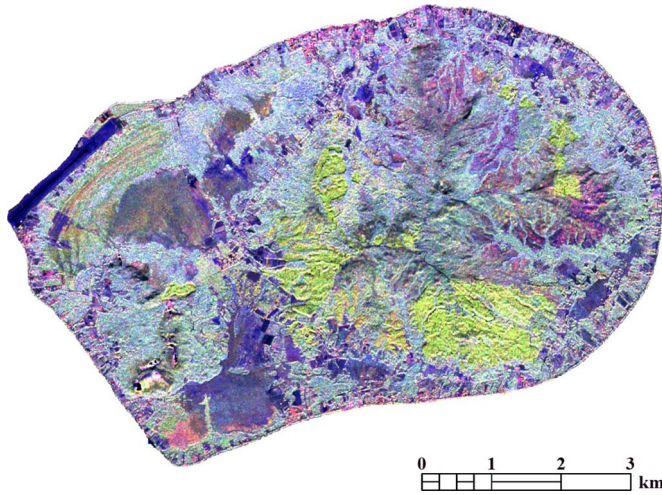


Fig. 2. AIRSAR image of the Tubuai Island. The RGB channels correspond respectively to intensities in  $hh$  and  $h\nu$  polarization at L-band and  $\nu\nu$  polarization at C-band.



Fig. 3. Quickbird image of the Tubuai Island.

in order to approach realistic backscattering coefficient values over densely forested areas. An AIRSAR composite red, green, and blue (RGB) image of the Tubuai island is shown in Fig. 2.

In order to reduce speckle, a polarimetric filter has been applied using a  $5 \times 5$  sliding window [31]. Then, all the polarimetric indicators have been estimated over a  $5 \times 5$  local neighborhood over the filtered data. The  $5 \times 5$  pixel size of the neighborhood has been retained in order to preserve the spatial resolution, although it may induce some bias in the estimation of the different polarimetric parameters [32].

2) *Quickbird Image*: In support to *in situ* measurements, an optical image has been acquired in June 2004 by the sensor onboard the Quickbird satellite, in four spectral bands (blue, green, red, and near infrared), each with a spatial resolution of 2.5 m. The image is shown in Fig. 3.

### C. Experimental Results

The classification methods (Wishart or SVM) are applied for the seven classes given in Table II. The ground surveys allowed the definition of different regions of interest, which are representative of each class. After the removal of borders and

possible relief artifacts, their corresponding area is ranging between 750 and 225 000 m<sup>2</sup>, with an average of about 11 300 m<sup>2</sup> (i.e., 30, 9000, and 450 AIRSAR pixels, respectively). For a given class, all the regions are merged, and pixels are randomly divided into two distinct subsets for training and control samples whose sizes are given Table II. For classification runtime consideration, the maximum numbers of training and control samples for a given class do not exceed 3000 and 5000, respectively. There are less training points than control points for computation time considerations and robustness characterization. The same training samples are retained whatever the classification method chosen.

The classification accuracy is given by the mean producer accuracy (MPA) that represents the mean of the producer accuracy (expressed in percent) of the seven classes [33]. This parameter is chosen because it puts the emphasis on the discrimination quality between each class rather than on the overall number of well-classified pixels. Consequently, it is more relevant when the classes under consideration have critically different number of pixels, as occurring in the present study case. For example, the Guava specie, which is represented by only 1000 pixels and is rather difficult to detect, is, however, particularly watched on.

1) *Configuration of the SVM Kernel*: The SVM algorithm is developed with the Libsvm library [34]. Lin and Lin [35] state that the sigmoid kernel is not better than the RBF kernel in general. On the other hand, several tests show that the polynomial kernel leads to significantly more computational time than the RBF kernel. For example, with a 3<sup>rd</sup> polynomial kernel, one classification run takes 40 times longer than one SVM classification run with an RBF kernel (about 3 h versus 5 min, respectively). Consequently, the RBF kernel has been chosen for this paper. Fig. 4(a) shows the influence of the cost  $C$  and the  $\sigma$  parameters on the classification accuracy (MPA) for a vector  $V\_WISH$  defined by the nine real elements of the L-band coherency matrix. It appears that the classification performance increases with decreasing values of  $\sigma$ . For  $\sigma \leq 1$ , the classification shows similar performance, particularly for large  $C$  values.

Fig. 4(b) shows a vector defined by 45 polarimetric indicators (the 45 first parameters given in Table IV). Contrary to Fig. 4(a), the classification performance increases with  $\sigma$ , with the maximum classification accuracy observed for  $\sigma \geq 0.3$ . This is in concordance with Vapnik [36], who recommends increasing  $\sigma$  value with the number of considered primitives. Moreover, the influence of  $C$  on the MPA appears in that case to be negligible. These results show that the values defining the optimum RBF kernel and cost parameter are dependent of the involved vector dimension. However, for simplification purposes, we choose, for any considered vector in this paper, the RBF kernel with  $\sigma = 0.5$  and  $C = 1000$ . It can be noticed that this good compromise between the two cases shown Fig. 4 is the same parameterization as [37].

2) *Comparison Between Wishart and SVM Classifications*: In order to evaluate the potential of the SVM method, a comparison is first conducted with a supervised Wishart classifier based on the *a priori* knowledge of the statistical properties of the coherency matrix elements [5]. In order to conduct a fair comparison between SVM and Wishart classifiers, the SVM classification considers here a vector, denoted by  $V\_WISH$ ,

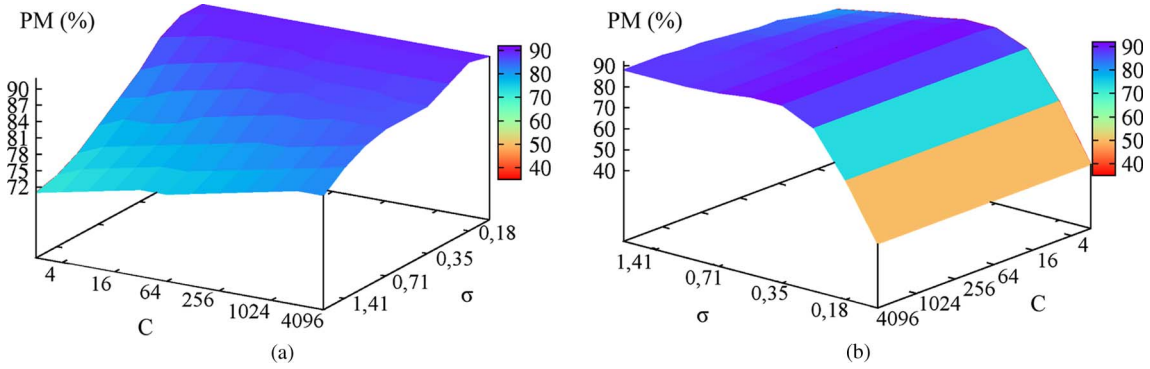


Fig. 4. Classification accuracy (MPA) using the SVM method with the RBF kernel versus the cost ( $C$ ) and  $\sigma$  parameters. (a) For the nine-component  $V\_WISH$  vector. (b) For the 45-component vector (the 45 first polarimetric indicators given Table IV) for L-band data.

TABLE III  
COMPARISON OF THE MPA (IN PERCENT) OBTAINED FROM SVM WITH  
THE VECTOR  $V\_WISH$  AND WISHART CLASSIFICATIONS

Type	Class	L Band		P band		L + P + C bands	
		Wishart	SVM	Wishart	SVM	Wishart	SVM
Forest	Pinus	32	74	56	71	81	99
	Falcata	69	80	37	64	75	99
	Purau	48	78	61	85	75	98
	Guava	76	88	66	74	74	100
Low vegetation	Fernland	62	93	49	88	56	98
	Swampy vegetation	85	97	92	93	95	99
	Bare soil	90	98	91	96	91	99
overall performance (MPA)		66	87	62	82	78	99

including only the nine elements of the coherency matrix (i.e., the three real diagonal elements and the real and imaginary parts of the three off-diagonal elements). In addition, the comparison has also been made when the L-, P-, and C-bands are combined together. In that case, the vector used for the SVM algorithm, denoted by  $V\_WISH\_PLC$ , includes 19 elements, i.e., the  $2 \times 9$  elements of the coherency matrix of L- and P-bands, with the addition of the intensity  $I_{\nu\nu}$  acquired at C-band. The results are given Table III. In general, the SVM algorithm gives much better results than those obtained with the Wishart classifier, with MPA values of 87% and 82% for L- and P-bands, which are about 20% higher than the Wishart classifier results. It can be noticed that the same SVM classification results are obtained by replacing in  $V\_WISH$  the real/imaginary parts by the amplitude/phase of the three off-diagonal elements.

The poor performance of the Wishart classifier is due to the discrepancy between the supposed Wishart distribution and the one observed by the experimental data. This is confirmed by the simulations of radar data, respecting both the Wishart distribution and the averaged coherency matrix observed over the different training classes. For this simulation data set, the Wishart classifier shows a better accuracy than the SVM algorithm, with, for example, at L-band, MPA values of 81% and

74%, respectively. The discrepancy of experimental data with the Wishart distribution is not surprising for the considered airborne data set, for which imaged surfaces are not homogeneous (with the presence of texture, for example) at such resolution cell size with respect to the wavelength. Similar figure case can also be expected with new spaceborne sensors, such as RADARSAT-2 or ALOS/PALSAR. For such situation, the SVM algorithm does not take into account any *a priori* information about the statistical distribution of the processed data. The good accuracy obtained with the experimental data indicates the potential of the nonlinear kernel theory for classification, for training data set which has to be the most representative of each class. The remarkable accuracy ( $MPA = 99\%$ ) obtained with the SVM method when the P, L, and C-bands are combined can be noted. The 99% MPA value observed, which is remarkably high, is not representative of reality, since a lot of approximations are made, such as reducing the numerous different landscapes to only seven pure classes. However, the relative differences between the classification accuracies are significant, since all are based on the same training and control classes.

On the other hand, the MPA values are about 5% higher for L-band than for P-band, whatever the classification method used. The analysis of different confusion matrices shows, as can be expected, that there is a higher confusion at P-band between the Fernland and swampy vegetation classes, i.e., the P-band is less sensitive to low vegetation densities. However, it is more difficult to give an interpretation about the behavior observed over forest classes. Despite better penetration capabilities in forest canopies at low frequencies, at the exception of Purau, a higher confusion between forest species is observed at P-band than at L-band.

The images corresponding to the classification obtained with Wishart and SVM classifiers when the P-, L-, and C-bands are combined are shown in Fig. 5. It is particularly obvious that the large number of pixels that are wrongly classified as Guava with the Wishart classification is significantly reduced with the SVM classification.

These results indicate that, although the SVM method is not particularly developed for radar data, it presents nevertheless a significant potential for radar polarimetric data classification.

a) *Polarimetric indicator contribution*: This section analyzes the contribution of the different polarimetric indicators listed in Section II-A (Table I) according to the greedy forward



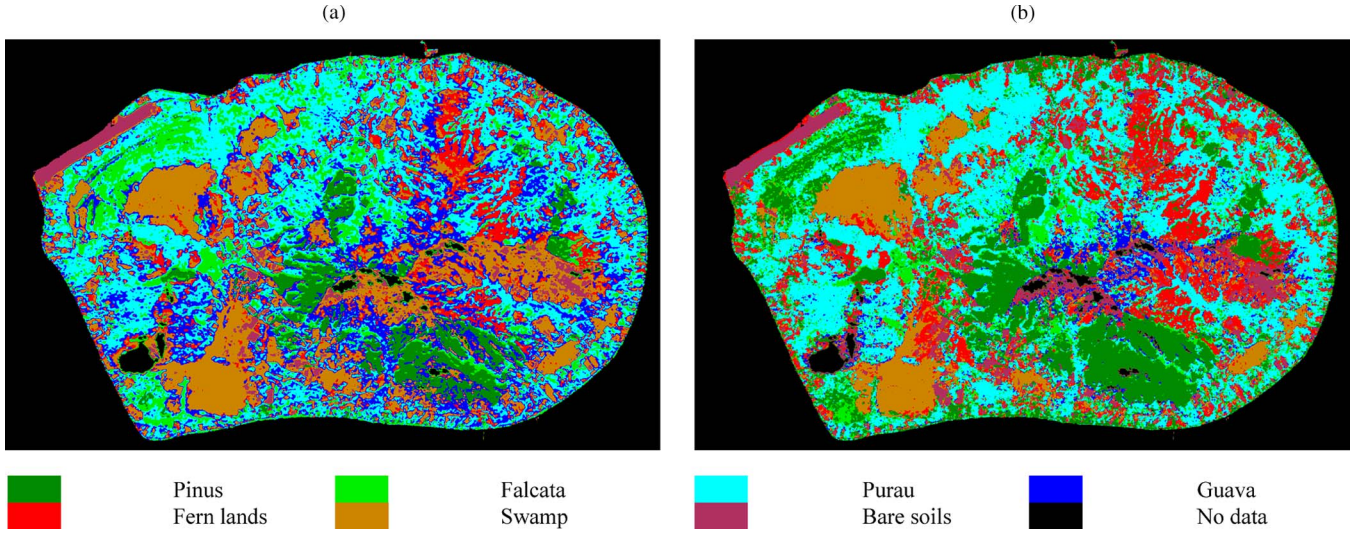


Fig. 5. Images of the classification obtained when P-, L-, and C-bands are combined. (a) Wishart classifier ( $MPA = 78\%$ ) and (b) SVM for the 19 indicators of the  $V\_WISH\_PLC$  vector ( $MPA = 99\%$ ).

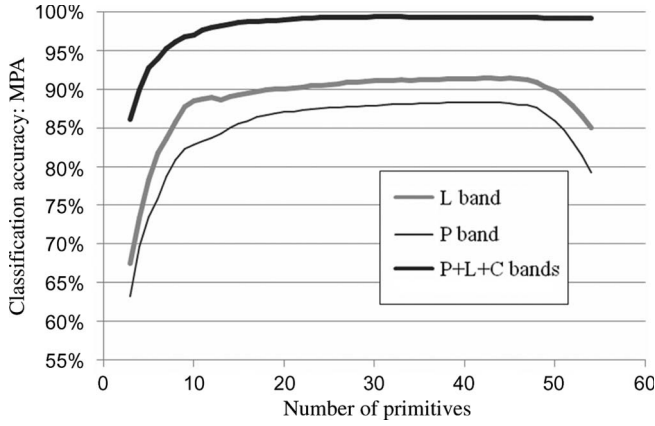


Fig. 6. Contribution of the polarimetric indicators for L-band, P-band, and when P-, L-, and C-bands are combined together. Details about the corresponding primitives at L- and P-bands are given in Table IV.

or backward methods applied to the SVM algorithm presented in Section II-C.

When only one single frequency polarimetric band is considered (i.e., L- or P-band), the 54 polarimetric indicators (listed in Table I) define a 54-component reference vector noted as  $V\_FULL$ . Fig. 6 shows the classification overall accuracy (MPA) with respect to the number of primitives. It is the result of the different steps of the greedy backward algorithm from the  $V\_FULL$  initial vector, at L- and P-bands. Table IV gives the details on the corresponding primitive ranking. Both L- and P-bands indicate a similar behavior: A large plateau around the MPA maximum value is reached for a number of primitives ranging approximately between 20 and 45. The MPA maximum values are 91% and 88% for L- and P-bands, respectively, representing gains of 4% and 6% by comparison with the results obtained with the  $V\_WISH$  vector. Below ten primitives, the classification performance shows a dramatic decrease (down to 63% and 67% for L- and P-bands) due to too reduced remnant information. It is also worth noting that a marked decrease (6% and 9% for L- and P-bands) is also observed for a primitive number higher than 48 for both bands, indicating that some polarimetric indicators introduce high confusion for classification.

TABLE IV  
RANKING OF THE DIFFERENT POLARIMETRIC INDICATORS FOR THE RESULTS BASED ON THE  $V\_FULL$  VECTOR SHOWN IN FIG. 6. THE SET OF PRIMITIVES CORRESPONDING TO THE NUMBER ( $5 \leq N \leq 54$ ) IS CUMULATIVE FROM THE FIVE FIRST PRIMITIVES (FIRST LINE)

Number of primitives	L Band	MPA (%)	P Band	MPA (%)
5	$I_{rr}, \alpha, \Re(T_{12}),  \rho_{ll-rr} , \Im(T_{13})$	78	$m,  \rho_{hh-vv} , I_{hh}/I_{vv}, a, I_{ll}/I_{rr}$	73
10	$\Im(T_{12}), I_{ll}/I_{rr}, \Re(T_{13}), c_{v-lr}, \Re(T_{23})$	88	$\phi_{v-hv}, c_{v-lb}, \phi_{hh-vv}, \Re(T_{23}), c_{v-vv}$	83
15	$c_{v-vv}, m,  \rho_{hh-hv} ,  \rho_{rr-lr} ,  \rho_{ll-lr} $	89	$ \rho_{vv-hv} ,  \rho_{rr-lr} ,  \rho_{hh-hv} ,  \rho_{ll-lr} , c_{v-hh}$	86
20	$I_{ll}, d_{-P_{max}}, c_{v-hh}, I_{hv}, I_{hh}$	90	$I_{min}, c_{v-rr}, c_{v-hv}, I_{vv}, \Re(T_{12})$	87
25	$\Delta(d_{-P}),  \rho_{vv-hv} , P_v, I_{hv}/I_{hh}, a$	91	$I_{hv}, I_{rr}/I_{lr}, \Re(T_{13}), c_{v-lr}, \alpha$	88
30	$ \rho_{hh-vv} , c_{v-ll}, \Im(T_{23}), T_{11}, T_{22}$	91	$P_v, P_s, I_{hv}/I_{hh}, \Im(T_{13}), T_{22}$	88
35	$\tau, I_{hh}/I_{vv}, I_{ll}/I_{rr}, I_{rr}/I_{lr}, \phi_{l-lr}$	91	$I_{hh}, \Im(T_{23}), I_{max}/I_{min}, H, S$	88
40	$I_{hv}/I_{vv}, I_{max}/I_{min}, P_d, P_s, H$	91	$I_{hv}/I_{vv}, I_{rr}, \Delta(d_{-P}), T_{11}, P_d$	88
45	$I_{min}, c_{v-hv}, I_{vv}, \phi_{hh-vv}, d_{-P_{min}}$	91	$I_{ll}, I_{ll}/I_{lr}, \Im(T_{12}),  \rho_{ll-rr} , d_{-P_{max}}$	88
50	$c_{v-rr}, S, V_s, \phi_{hh-hv}, \phi_{rr-lr}$	90	$d_{-P_{min}}, \phi_{hh-hv}, \tau, \phi_{rr-lr}, \phi_{l-lr}$	86
54	$\phi_{ll-rr}, \psi, \phi_{v-hv}, \gamma$	85	$\phi_{ll-rr}, \psi, \gamma, v$	79

cation. An analysis of Table IV shows that seven particular indicators are among the less discriminative both for L- and P-bands: four of the Euler parameters  $\nu, \psi, \gamma$ , and  $\tau$  and the three phases of the degrees of coherence  $\phi_{ll-rr}, \phi_{rr-lr}$ , and  $\phi_{hh-hv}$ . It is not surprising, as the Euler parameter are particularly defined to account for the characterization of deterministic target inducing fully polarized radar response, which is not the case over vegetated surfaces. The nonefficiency of the phases

of the degrees of coherence is also expected over these dense vegetated areas, although useful information can be extracted from some of these parameters over other types of surface, such as urban or spared vegetation areas [38]–[40]. On the other hand, polarimetric indicators occupying the left part of the curve are not necessarily the most significantly discriminating ones. This is due to the constant performance of the classification on the plateau region, which indicates that each individual indicator has a negligible contribution. Consequently, in that horizontal part of the curve, the greedy backward method can remove indicators with more intrinsic discriminating behavior than others (see, for example, the entropy  $H$  with regard to  $\varphi_{\nu\nu-h\nu}$  at P-band).

Moreover, it has to be pointed out that the greedy algorithms are depending on the original subset of primitives (defining the initial vector), as well as the subset that is investigated to add or remove the indicator at the next iteration. For example, a forward approach with the initial vector defined by the first five primitives (first line of Table IV) would give a different ranking. Several tests (not shown here) have illustrated this behavior; however, the resulting curves are similar to those shown in Fig. 6, confirming that a different combination of indicators can give similar performance. In particular, a greedy forward analysis based on  $V\_WISH$  initial vector shows that the addition of different coefficients of variation, intensity channels (or ratio or Freeman parameters), as well as the entropy, allows one to obtain the same maximum classification accuracy.

These results show that, even if good classification results are obtained when only the elements of the coherency matrix are considered, the addition of other polarimetric indicators contributes to a systematic improvement of the classification accuracy of 5% and 7% for L- and P-bands. Furthermore, the greedy backward method allows one to point out some confusing indicators leading to a reduction of the classification results (the Euler parameters  $\nu$ ,  $\psi$ ,  $\gamma$ , and  $\tau$  and the three phases of the degrees of coherence  $\varphi_{ll-rr}$ ,  $\varphi_{rr-lr}$ , and  $\varphi_{hh-h\nu}$ ), although, as already mentioned, it does not allow a deeper comparison between the different indicators.

Concerning the contribution of the combination of P-, L-, and C-bands, the MPA value obtained when all the 110 parameters are combined (i.e.,  $2 \times 54$  at L- and P-bands with the addition of  $I_{\nu\nu}$  and  $c_{\nu-\nu\nu}$  at C-band) is 57%, indicating the high degree of confusion introduced here again by different polarimetric indicators. A similar greedy backward analysis from these 110 existing primitives cannot be considered due to computational time constraint. As an illustration, about 53 h is needed on a Pentium4 630–3.0-GHz processor to remove one among 100 primitives. Consequently, the results shown in Fig. 6 are based on the initial 19-component vector  $V\_WISH\_PLC$ , the right and left parts of the curve resulting from greedy forward and backward analyses, respectively. The addition of other polarimetric indicators to  $V\_WISH\_PLC$  does not improve the classification results, which observe a constant MPA value of 99% (as far as the 54 indicators shown here are considered). Details about these different indicators (which are mostly intensity parameters) are not given, as the plateau observed here again hampers one to evaluate more deeply their discriminating contribution.

#### IV. CONCLUSION

This paper has addressed the potential of SVM algorithm for the classification of polarimetric SAR data. The SVM algorithm is particularly suited to account for numerous and heterogeneous parameters, which enables to take into account a large bunch of polarimetric indicators. The proposed method has been applied to data that have been acquired over a French Polynesian island during an AIRSAR mission. When only the elements of the coherency matrix are involved, the SVM algorithm gives a good overall accuracy with MPA values of 87% for L-band, 82% for P-band, and 99% when L-, P-, and C-bands are combined. It represents a high improvement of about 20% by comparison with the Wishart classification. These results indicate that the theoretical Wishart distribution is obviously not observed by the experimental data, while by contrast, no *a priori* information is required for the SVM algorithm. Such a discrepancy between experimental radar data and the Wishart distribution may be observed not only for airborne data but also with the last polarimetric spaceborne sensors (ALOS-PALSAR or RADARSAT-2, for example), characterized by a rather high-resolution cell size with respect to the wavelength, for which imaged areas are not homogeneous. The addition of polarimetric indicators allows an improvement of about 5% of the results ( $MPA = 91\%$  and  $88\%$  for L- and P-bands, respectively) with respect to those involving the coherency matrix elements. As a consequence, a recommendation for optimal use would be to consider only the elements of the coherency matrix for the SVM classification, which shows a good compromise between the number of involved polarimetric indices and the classification accuracy obtained. The greedy analysis performed allowed one to clearly point out polarimetric indicators introducing significant confusion in the classification at both L- and P-bands. These are the Euler parameters and three differential phases of the degree of coherence, which is not surprising over such dense vegetative area. However, the greedy algorithm does not allow drawing conclusion about the most discriminating parameters. Nevertheless, these results have demonstrated the high potential of the SVM algorithm for radar-polarimetric-data-supervised classification. Additional analyses have to be performed in the future, in particular, to assess more precisely the influence of the kernel used in the SVM method.

#### ACKNOWLEDGMENT

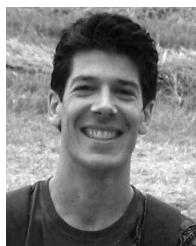
The authors would like to thank J.-Y. Meyer for his help during the survey mission, the Government of French Polynesia and its Urbanism Department for providing the AirSAR and Quickbird data required for this paper, and the anonymous reviewers for their valuable comments which improved the quality of this paper.

#### REFERENCES

- [1] A. Freeman and S. L. Durden, "A three-component scattering model for polarimetric SAR data," *IEEE Trans. Geosci. Remote Sens.*, vol. 36, no. 3, pp. 963–973, May 1998.
- [2] E. Krogager, "New decomposition of the radar target scattering matrix," *Electron. Lett.*, vol. 26, no. 18, pp. 1525–1527, Aug. 1990.



- [3] S. R. Cloude and E. Pottier, "An entropy based classification scheme for land applications of polarimetric SAR," *IEEE Trans. Geosci. Remote Sens.*, vol. 35, no. 1, pp. 68–78, Jan. 1997.
- [4] A. A. Swartz, H. A. Yueh, J. A. Kong, L. M. Novak, and R. T. Shin, "Optimal polarizations for achieving maximum contrast in radar images," *J. Geophys. Res.*, vol. 93, no. B12, pp. 15 252–15 260, Dec. 1988.
- [5] J. S. Lee, M. R. Grunes, and R. Kwok, "Classification of multi-look polarimetric SAR imagery based on complex Wishart distribution," *Int. J. Remote Sens.*, vol. 15, no. 11, pp. 2299–2311, Jul. 1994.
- [6] J. S. Lee, M. R. Grunes, E. Pottier, and L. Ferro-Famil, "Unsupervised terrain classification preserving polarimetric scattering characteristics," *IEEE Trans. Geosci. Remote Sens.*, vol. 42, no. 4, pp. 722–731, Apr. 2004.
- [7] F. Del Frate and D. Solimini, "On neural network algorithm for retrieving forest biomass from SAR data," *IEEE Trans. Geosci. Remote Sens.*, vol. 42, no. 1, pp. 24–34, Jan. 2004.
- [8] A. Freeman, J. Villaseñor, J. D. Klein, P. Hoogeboom, and J. Groot, "On the use of multi-frequency and polarimetric radar backscatter features for classification of agricultural crops," *Int. J. Remote Sens.*, vol. 15, no. 9, pp. 1799–1812, Jun. 1994.
- [9] L. J. Du, J. S. Lee, K. Hoppel, and S. A. Mango, "Segmentation of SAR image using the wavelet transform," *Int. J. Imaging Syst. Technol.*, vol. 4, pp. 319–329, 1992.
- [10] L. E. Pierce, F. T. Ulaby, K. Sarabandi, and M. C. Dobson, "Knowledge-based classification of polarimetric SAR images," *IEEE Trans. Geosci. Remote Sens.*, vol. 32, no. 5, pp. 1081–1086, Sep. 1994.
- [11] G. Grandjean, P. Paillou, P. Dubois-Fernandez, T. August-Bernex, N. N. Baghdadi, and J. Achache, "Subsurface structures detection by combining L-band polarimetric SAR and GPR data: Example of the Pyla Dune (France)," *IEEE Trans. Geosci. Remote Sens.*, vol. 39, no. 6, pp. 1245–1258, Jun. 2001.
- [12] F. Mattia, T. Le Toan, J.-C. Souyris, G. De Carolis, N. Floury, F. Posa, and G. Pasqueriello, "The effect of surface roughness on multifrequency polarimetric SAR data," *IEEE Trans. Geosci. Remote Sens.*, vol. 35, no. 4, pp. 954–966, Jul. 1997.
- [13] R. Touzi, S. Goze, T. Le Toan, A. Lopes, and E. Mougin, "Polarimetric discriminators for SAR images," *IEEE Trans. Geosci. Remote Sens.*, vol. 30, no. 5, pp. 973–980, Sep. 1992.
- [14] C. J. Burges, "A tutorial on support vector machines for pattern recognition," in *Data Mining Knowledge Discovery*, U. Fayyad, Ed. Norwell, MA: Kluwer, 1998.
- [15] C. Tison, N. Pourthié, and J.-C. Souyris, "Target recognition in SAR images with support vector machine (SVM)," in *Proc. IGARSS*, Barcelona, Spain, Jul. 2007, pp. 456–459.
- [16] G. Mercier and F. Girard-Ardhuin, "Unsupervised oil slick detection by SAR imagery using kernel expansion," in *Proc. IGARSS*, Jul. 2005, vol. 1, pp. 494–497.
- [17] J. S. Lee and K. Hoppel, "Principal components transformation of multifrequency polarimetric SAR imagery," *IEEE Trans. Geosci. Remote Sens.*, vol. 30, no. 4, pp. 686–696, Jul. 1992.
- [18] S. R. Cloude and E. Pottier, "A review of target decomposition theorems in radar polarimetry," *IEEE Trans. Geosci. Remote Sens.*, vol. 34, no. 2, pp. 496–518, Mar. 1996.
- [19] B. Hapke, "Coherent backscatter and the radar characteristics of outer planet satellites," *Icarus*, vol. 88, no. 2, pp. 407–417, Dec. 1990.
- [20] F. T. Ulaby and C. Elachi, *Radar Polarimetry for Geoscience Applications*. Norwood, MA: Artech House, 1990, p. 15.
- [21] J. R. Huynen, "Phenomenological theory of radar targets," Ph.D. dissertation, Delft Univ., Delft, The Netherlands, 1970.
- [22] D. Laurent, E. Pottier, and J. Saillard, "The Euler vector: A polarimetric descriptor of the ocean surface," *J. Electromagn. Waves Appl.*, vol. 9, no. 1/2, pp. 217–240, 1995.
- [23] R. Touzi and A. Lopes, "Statistics of the Stokes parameters and of the complex coherence parameters in one-look and multilook speckle fields," *IEEE Trans. Geosci. Remote Sens.*, vol. 34, no. 2, pp. 519–531, Mar. 1996.
- [24] C. Oliver and S. Quegan, *Synthetic Aperture Radar Images*. Norwood, MA: Artech House, 1998.
- [25] J. A. Kong, A. Swartz, H. A. Yueh, L. M. Noval, and R. T. Shin, "Identification of terrain cover using the optimum polarimetric classifier," *J. Electromagn. Waves Appl.*, vol. 2, no. 2, pp. 171–194, 1988.
- [26] C.-W. Hsu and C.-J. Lin, "A comparison of methods for multiclass support vector machines," *IEEE Trans. Neural Netw.*, vol. 15, no. 2, pp. 415–425, Mar. 2002.
- [27] I. Guyon, J. Weston, S. Barnhill, and V. Vapnik, "Gene selection for cancer classification using support vector machines," *Mach. Learn.*, vol. 46, no. 1–3, pp. 389–422, Jan. 2002.
- [28] J. J. Van Zyl and A. Chu, *AIRSAR Integrated Processor Documentation—Data Formats*, Jun. 9, 2003, ver. 0.17. [Online]. Available: [http://airsar.jpl.nasa.gov/data/data\\_format.pdf](http://airsar.jpl.nasa.gov/data/data_format.pdf)
- [29] J. J. Van Zyl, "Calibration of polarimetric radar images using only image parameters and trihedral corner reflector responses," *IEEE Trans. Geosci. Remote Sens.*, vol. 28, no. 3, pp. 337–348, May 1990.
- [30] H. A. Zebker, J. J. Van Zyl, and D. N. Held, "Imaging radar polarimetry from wave to synthesis," *J. Geophys. Res.*, vol. 92, no. B1, pp. 683–701, 1987.
- [31] J.-S. Lee, M. R. Grunes, and G. de Grandi, "Polarimetric SAR speckle filtering and its implication for classification," *IEEE Trans. Geosci. Remote Sens.*, vol. 37, no. 5, pp. 2363–2373, Sep. 1999.
- [32] C. Lopez-Martinez and X. Fabregas, "Model-based polarimetric SAR speckle filter," *IEEE Trans. Geosci. Remote Sens.*, vol. 46, no. 11, pp. 3894–3907, Nov. 2008.
- [33] W. G. Rees, *Physical Principles of Remote Sensing*, 2nd ed. Cambridge, U.K.: Cambridge Univ. Press, 2001, p. 301.
- [34] C.-C. Chang and C.-J. Lin, *A Library for Support Vector Machine*, 2008. [Online]. Available: <http://www.csie.ntu.edu.tw/~cjlin/libsvm>
- [35] H.-T. Lin and C.-J. Lin, "A study on sigmoid kernels for SVM and the training of non-PSD kernels by SMO-type methods," Dept. Comput. Sci., Nat. Taiwan Univ., Taipei, Taiwan, Tech. Rep., 2003.
- [36] V. N. Vapnik, "Statistical learning theory," in *SV Machines for Pattern Recognition*. John Wiley & Sons, 1998, ch. 12, pp. 496–498.
- [37] S. Fukuda and H. Hirokawa, "Support Vector Machine classification of land cover: Application to polarimetric SAR data," in *Proc. IGARSS*, Jul. 2001, vol. 1, pp. 187–189.
- [38] M. Jäger, M. Neumann, S. Guillaso, and A. Reigber, "A self-initializing PolInSAR classifier using interferometric phase differences," *IEEE Trans. Geosci. Remote Sens.*, vol. 45, no. 11, pp. 3503–3518, Nov. 2007.
- [39] T. Moriyama, S. Uratsuka, T. Umehara, M. Satake, A. Nadai, H. Maeno, K. Nakamura, and Y. Yamaguchi, "A study on extraction of urban areas from polarimetric synthetic aperture radar image," in *Proc. IGARSS*, Anchorage, AK, Sep. 2004, pp. 703–706.
- [40] J. S. Lee, D. L. Schuler, and T. L. Ainsworth, "Polarimetric SAR data compensation for terrain azimuth slope variation," *IEEE Trans. Geosci. Remote Sens.*, vol. 38, no. 5, pp. 2153–2163, Sep. 2000.



**Cédric Lardeux** was born in 1980. He received the M.S. and Ph.D. degrees in science of geographic information from the Université Paris-Est Marne-la-Vallée, Marne-la-Vallée, France, in 2005 and 2008, respectively.

He is currently in a Postdoctoral position with the SAPHIR Team, Université de Rennes, Rennes, France, where he is involved in radar polarimetry for the cartography of tropical vegetation.



**Pierre-Louis Frison** received the M.S. degree in astrophysics, geophysics, and spatial techniques and the Ph.D. degree from the University Paul Sabatier, Toulouse, France, in 1993 and 1997, respectively.

Since 1999, he has been an Associated Professor with the Université Paris-Est Marne-la-Vallée, Marne-la-Vallée, France. He works on the remote sensing of earth surfaces with radar sensors, including SAR and scatterometers.



**Céline Tison** received the Engineering and Ph.D. degrees from the Ecole Nationale Supérieure des Télécommunications, Paris, France, in 2001 and 2004, respectively.

She is currently with the Altimetry and Radar Department, Centre National d'Etudes Spatiales, Toulouse, France. Her main research interest includes synthetic aperture radar image information extraction, particularly in the framework of high-resolution urban imagery and high-resolution interferometry and polarimetry.



**Jean-Claude Souyris** received the Engineering degree in electronics from l'Ecole Nationale Supérieure d'Électrotechnique, d'Électronique, d'Informatique et d'Hydraulique de Toulouse, Toulouse, France, in 1989 and the Ph.D. degree from the Université Paul Sabatier, Toulouse, in 1992.

In 1994, he was a Visiting Scientist with the Center for Electromagnetic Theory and Applications, Massachusetts Institute of Technology, Cambridge. Since 1997, he has been with the Centre National d'Etudes Spatiales, Toulouse, where he is currently

the head of the altimetry and radar department. He has authored or coauthored several articles dedicated to radar image processing, radar polarimetry, and radar altimetry. He also coauthored (with D. Massonnet) the book *Imaging with Synthetic Aperture Radar*.

Dr. Souyris served as the Technical Chairman of the 2003 International Geoscience and Remote Sensing Symposium.



**Benoît Stoll** received the Ph.D. degree in signal processing (blind source separation) from the University of Toulon-Var, Nice, France, in 2000.

After receiving the Ph.D. degree, he moved temporarily to the Laboratoire des Images et des Signaux, Grenoble, France, to continue his work. In 2001, he joined the Terre-Ocean Laboratory (now Laboratoire des Geosciences du Pacifique Sud), French Polynesia University, Tahiti, Polynésie Franse, to study the complex Polynesian Islands vegetation on satellite images using remote-sensing

techniques. His fields of investigations are the remote sensing of high islands vegetation covers, atolls, and coconut fields based on optical and radar high-resolution images.



**Bénédicte Fruneau** received the B.S. degree in electrical engineering and the M.Sc. degree in image and signal processing from the Grenoble Institute of Technology, Grenoble, France, in 1991 and the Ph.D. degree in geophysics from the University of Paris 7, Paris, France, in 1995.

Since 1996, she has been with the Université de Marne-la-Vallée, Marne-la-Vallée, France, where she is currently an Assistant Professor. Her research activities are principally dedicated to the measurement and the analysis of surface deformation associ-

ated with natural and anthropogenic phenomena in various contexts using SAR differential interferometry.



**Jean-Paul Rudant** received the Agregation in physics in 1969 and the Ph.D. degree in geophysics from the University of Paris 6, France, in 1974.

He is currently a Professor with the Université Paris-Est Marne-la Vallée, Marne-la Vallée, France, and the Head of the Earth Observation team. His experience covers geophysics and remote sensing. He supervises the Geographical Information Master, coempowered with the Ecole Nationale des Sciences Géographiques. He has invested in numerous programs with space agencies (Centre National

d'Etudes Spatiales, European Space Agency, and the National Space Development Agency of Japan) involving radar images.